Dislocation/void interactions: Comparing a multi-principal element alloy with its constituent pure metal

Anshu Raj [a], Weisen Ji [b], Shuozhi Xu [a] [ID],*

[a] School of Aerospace and Mechanical Engineering, University of Oklahoma, Norman, OK 73019-1052, USA
[b] Independent Researcher, San Jose, CA 95132, USA

ARTICLE INFO

ABSTRACT

Multi-principal element alloys (MPEAs), characterized by the near-equiatomic mixing of three or more principal elements, exhibit a high configurational entropy that stabilizes solid solution phases and yields outstanding mechanical properties such as high strength, ductility, and toughness. While chemical complexity contributes significantly to these enhanced properties, incorporating nanostructural obstacles like voids offers an additional pathway for mechanical performance optimization. In this study, we employ the face-centered cubic $Al_{0.3}CoCrFeNi$ MPEA as a representative system to investigate dislocation-void interactions. One constituent pure metal, Ni, is also studied as a reference. We systematically examine the influence of void radius on the critical resolved shear stress (CRSS), revealing that, compared with Ni, the CRSS in the MPEA exhibits greatly reduced sensitivity to void size. In addition, the CRSS for the edge dislocation is higher than that for the screw dislocation in the MPEA, in contrast to Ni. These results highlight the role of nanostructural engineering in modulating dislocation mechanics, offering valuable guidance for the rational design of next-generation structural materials with superior performance.

1. Introduction

Developing high-performance metallic alloys primarily relies on altering chemical compositions and microstructures by introducing foreign elements and crystallographic defects, respectively [1]. In traditional dilute alloys, a single principal element forms the matrix of the system with various additional elements to enhance particular properties [2]. It was believed that mixing multiple elements at near-equiatomic ratios would lead to multiple simple phases, stoichiometric intermetallic compounds, or amorphous metallic glasses, which are usually brittle [3]. Thus, traditional alloy development focused on the corners and edges, instead of the central region, of a multi-component phase diagram [4]. In 2004, some carefully chosen metallic compositions were found to form stable solid solution phases [5,6]. Since then, the field of multi-principal element alloys (MPEAs) has seen explosive development [7]. Currently, MPEAs are defined as alloys composed of three or more principal elements on simple underlying lattices such as face-centered cubic (FCC) or body-centered cubic (BCC) [8]. The outstanding mechanical properties of MPEA, including great high-temperature strengths, excellent cryogenic fracture toughness, as well

as superior resistance to irradiation, creep, wear, and corrosion, position them as ideal material candidates for demanding applications in the aerospace, automotive, energy, and defense industries [9,10].

Dislocation behavior plays a central role in governing plastic deformation in MPEAs, yet it differs significantly from that in pure metals due to the complex local chemical environments characteristics, such as lattice distortion and chemical short-range order (CSRO) [11,12]. These factors alter the dislocation glide landscape, resulting in comparable mobilities for screw and edge dislocations, in contrast to the pronounced anisotropy typical of conventional metals [13]. Among MPEAs, the Al–Co–Cr–Fe–Ni system stands out for its exceptional mechanical performance and compositional tunability. In $Al_xCoCrFeNi$ alloys, phase stability and deformation behavior are highly sensitive to the Al concentration, with FCC, BCC/B2, or mixed phases emerging as x increases [14,15]. While their mechanical properties have been widely characterized across various temperatures, the underlying physics responsible for their unique behavior remains elusive. To gain deeper insight, atomistic simulations have been extensively applied to study deformation mechanisms in this alloy family [16–18]. This work focuses on Al0.3CoCrFeNi, selected for its stable FCC structure and

* Corresponding author.
  E-mail address: shuozhixu@ou.edu (S. Xu).

favorable combination of strength, ductility, toughness, and resistance to creep and shear failure [19,20]. Its thermodynamic and mechanical properties have been investigated via atomistic simulations [21,22]. Recently, Raj et al. [23] applied molecular statics at 0 K to this alloy, revealing that the local slip resistance is lower for a short (≈ 1 nm) screw dislocation than for an edge dislocation of similar length, in contrast to Ni, one of its constituent pure metals. In another study, Raj et al. [24] used a combination of molecular dynamics (MD) simulations at 5 K and statistical analyses to study the glide of a single, long (≈ 30 nm) dislocation. It was found that the critical resolved shear stress (CRSS) for the dislocation glide is slightly higher for the edge dislocation than for the screw dislocation, again in contrast to Ni.

Building on our previous work, the current study focuses on dislocation/void interactions. In ductile crystals, voids offer a simplified defect model without dislocation character, thereby avoiding the complexity of dislocation/dislocation reactions [25]. Their geometric simplicity makes them ideal for isolating and understanding fundamental mechanisms of dislocation obstruction [26]. Nevertheless, the atomic-level information is difficult to obtain because observing how dislocations interact with voids directly through *in situ* experiments is inherently difficult due to resolution and time constraints [27]. While elasticity theory provides partial insight into the interaction energetics, it does not fully capture the balance between the energy gain from eliminating the dislocation core and strain energy within the void, and the cost of forming a surface step as the dislocation shears through the cavity [28]. This balance governs the critical stress required for a dislocation to bypass a void, making the problem both physically significant and well-suited to atomistic modeling approaches [29–31].

Most atomistic simulations of dislocation/void interactions to date have been focused on pure metals. Simar et al. [32] and Cheng et al. [33] demonstrated through MD that void size, spacing, and loading conditions critically influence dislocation detachment behavior, particularly under dynamic and cyclic loading. The role of intrinsic stacking fault energy (ISFE) was systematically explored by Okita et al. [34], Hayakawa et al. [35], Asari et al. [36], and Doihara et al. [37], who showed that both ISFE and void geometry control depinning modes and the associated CRSS. Jian et al. [38] highlighted the sensitivity of dislocation/void interaction simulations to modeling parameters, while Jing et al. [39] combined MD and dislocation dynamics to assess helium bubble hardening, observing a weak dependence on bubble pressure and density. Hatano et al. [40] further revealed geometry- and temperature-dependent depinning mechanisms for both edge and screw dislocations in Cu, including cross-slip and prismatic loop formation.

In recent years, some progress has been made in understanding dislocation/void interactions in dilute alloys and MPEAs. Bahramyyan et al. [41] found that adding just 0.5 wt% Mg to Al significantly increased the Peierls stress and CRSS, altered the dislocation/void interaction mechanism compared to pure Al. They also showed that the Mg concentration strongly influenced dislocation mobility through both solute effects and thermal activation. Dou et al. [42] reported that dislocation motion is more difficult in Fe33Ni33Cr than in Fe10Ni20Cr due to larger fluctuations in ISFE. In addition, in Fe10Ni20Cr, voids can transform into stacking-fault tetrahedra at high temperatures, increasing obstacle strength, whereas sluggish diffusion in Fe33Ni33Cr suppresses this transformation, improving its resistance to irradiation hardening. Mei et al. [43] found that strong lattice mismatch in CoCrCuFeNi MPEA produces a friction stress roughly two orders of magnitude higher than in pure Cu and Ni, with both friction stress and local ISFE following a Gaussian distribution, leading to frequent changes in stacking fault width. They identified four distinct dislocation/microvoid interaction modes in this MPEA. Additionally, Vaid et al. [44] studied the interactions between edge dislocations and periodic arrays of voids in CrFeNi, determining the CRSS values for edge dislocations with different periodicity lengths using square voids with a side length
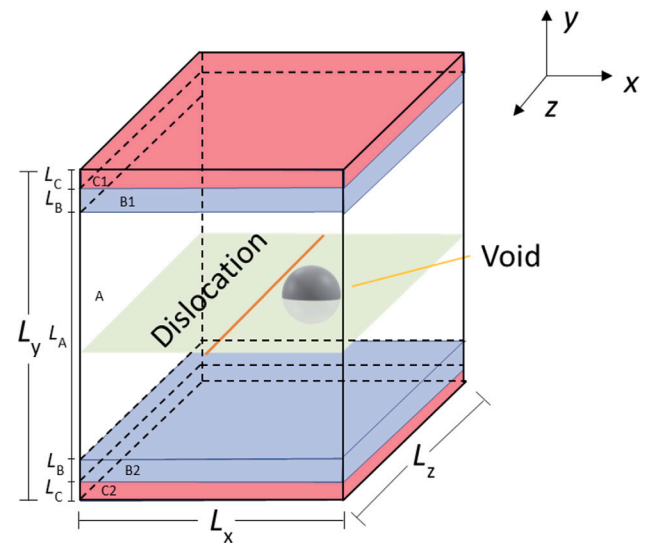

Fig. 1. Schematic of the simulation cell for dislocation/void interactions.

Table 1
Number of atoms deleted from the original simulation cell to create a void with different sizes in Ni and the MPEA.

Void radius (nm)	MPEA		Ni	
	Edge	Screw	Edge	Screw
4.8	42,485	42,451	43,217	43,196
3.6	17,509	17,464	17,778	17,773
2.4	5196	5178	5274	5261
1.2	648	646	654	656
0.6	81	79	81	80

of 5 nm. These studies typically considered only one type of dislocation – either edge or screw – and mostly only a single void size.

This paper investigates how a single dislocation interacts with a void in FCC $Al_{0.3}CoCrFeNi$. Compared with all prior work, the present study takes a more comprehensive approach, examining both edge and screw dislocations and their interactions with voids of different sizes. In addition, one constituent pure metal, Ni, is also analyzed here to provide references. As such, the present work enables deeper insights into the role of chemical complexity on dislocation/void interactions.

2. Methods

The embedded-atom method interatomic potential developed by Farkas and Caro [45] is used. In a recent study, we showed that this potential offers accurate values of lattice parameter, elastic constants, and ISFE of $Al_{0.3}CoCrFeNi$, as compared with an *ab initio* model or experimental data [23]. Atomistic simulations are conducted using LAMMPS [46]. Atomsk [47] is used to build the initial atomistic structures in both Ni and MPEA. Additionally, OVITO [48] is utilized for visualization and more detailed dislocation analysis.

Fig. 1 shows the simulation cell used to explore how a dislocation interacts with a void. An edge or a screw dislocation is introduced in the center of the simulation cell. For the edge dislocation, the x-, y-, and z-axes align with $[\bar{1}10]$, $[111]$, and $[11\bar{2}]$ directions, respectively, while for the screw dislocation they align with $[\bar{1}\bar{1}2]$, $[111]$, and $[\bar{1}10]$, respectively. Periodic boundary conditions are applied on the x and z axes, while a traction-free boundary is along the y axis. The simulation cell measures $L_x \approx 40$ nm, $L_y \approx 50$ nm, and $L_z \approx 30$ nm, containing over 5.5 million atoms.

It follows that a spherical void is added to the cell so that its center lines up with the mid-y and mid-z planes, and it is located at $0.15L_x$ from the right boundary of the cell. Five void radii are considered:
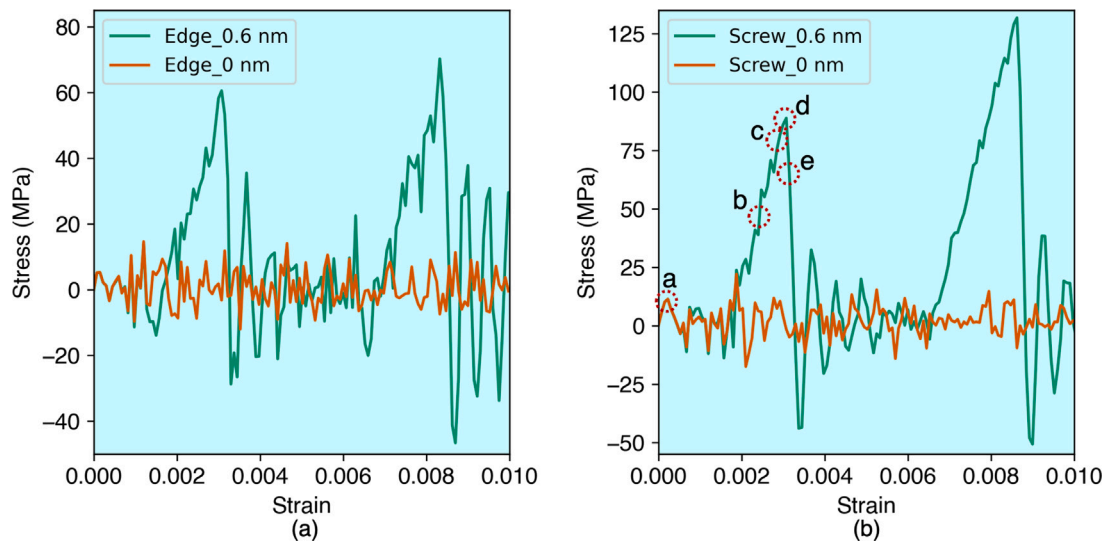
Fig. 2. Stress–strain curves for (a) an edge and (b) a screw dislocation interacting with a void with a radius of 0.6 nm in Ni. The curves for the void-free cases are also shown and labeled as "0 nm".
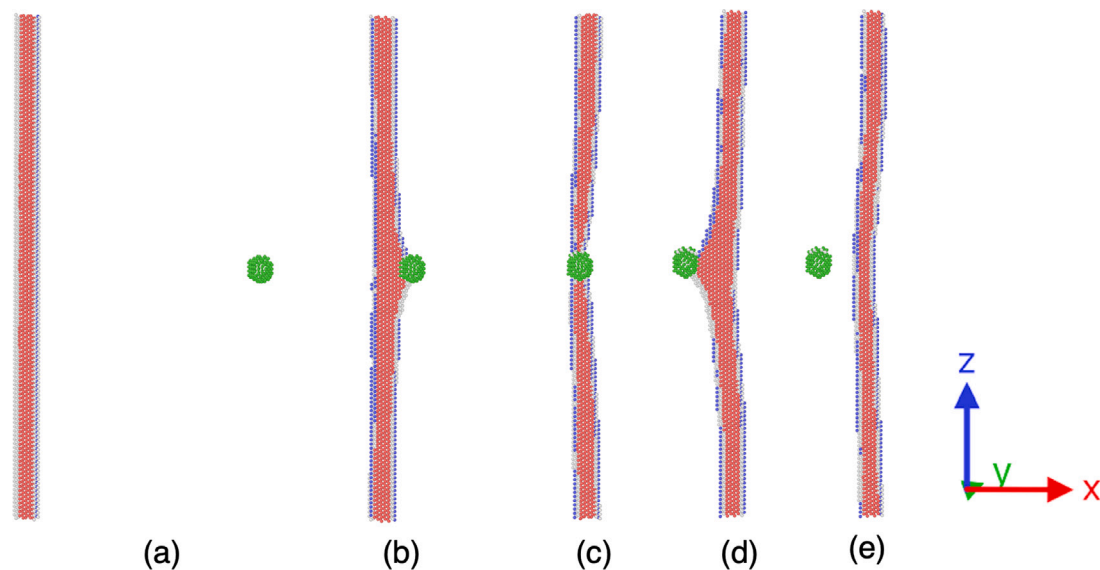

Fig. 3. A series of configurations of a screw dislocation interacting with a void with a radius of 0.6 nm in Ni, corresponding to selected points on the green stress–strain curve in Fig. 2(b).

0.6 nm, 1.2 nm, 2.4 nm, 3.6 nm, and 4.8 nm. This configuration ensures that the dislocation remains sufficiently distant from the void, preventing immediate interactions at the onset of dislocation motion. All atoms are randomly distributed in accordance with their compositional ratios, without any CSRO. The same void sizes in Ni are also studied to provide references. The lattice parameters for Ni and the MPEA are 3.52 and 3.55 Å, respectively. The numbers of atoms deleted to create voids are listed in Table 1.

Along the y axis, the simulation cell is divided into five regions: A, B1, B2, C1, and C2, as shown in Fig. 1. The thicknesses of C1 and C2 are equal and denoted as L_C, and those of B1 and B2 are equal and denoted as L_B. To prevent atoms in A, B1, and B2 from being influenced by the traction-free boundaries, L_C is chosen to exceed the cutoff distance of the interatomic potential. A constant applied strain rate of 10^7 s^{-1} is imposed with flexible boundary conditions in C1 and C2 to drive the dislocation motion. No thermostat is applied to A, C1, or C2 so as to not interfere with the flexible boundary conditions in C1 and C2, as well as dislocation dynamics in A. An NVT ensemble is applied to B1 and B2 to keep the temperature at 5 K.

To account for the randomness in atomic distribution in the MPEA, five MD simulations of dislocation/void interactions are conducted using five different atomic structures for each dislocation type and void size. The average CRSS among the five is reported in what follows.

3. Results and discussion

3.1. Ni

The stress–strain curves for a single dislocation interacting with a 0.6 nm void in Ni are shown in Fig. 2, with selected dislocation configurations highlighted in Fig. 3. The curves for the dislocation glide in a void-free lattice are also shown in Fig. 2. For the 4.8 nm void, the stress–strain curves are presented in Fig. 4, and the selected dislocation configurations are illustrated in Figs. 5 and 6. For both edge and screw dislocations, the stress first decreases below zero as the dislocation moves toward the void attracted by its traction-free surface and then rises nearly linearly with increasing strain. During this process, the
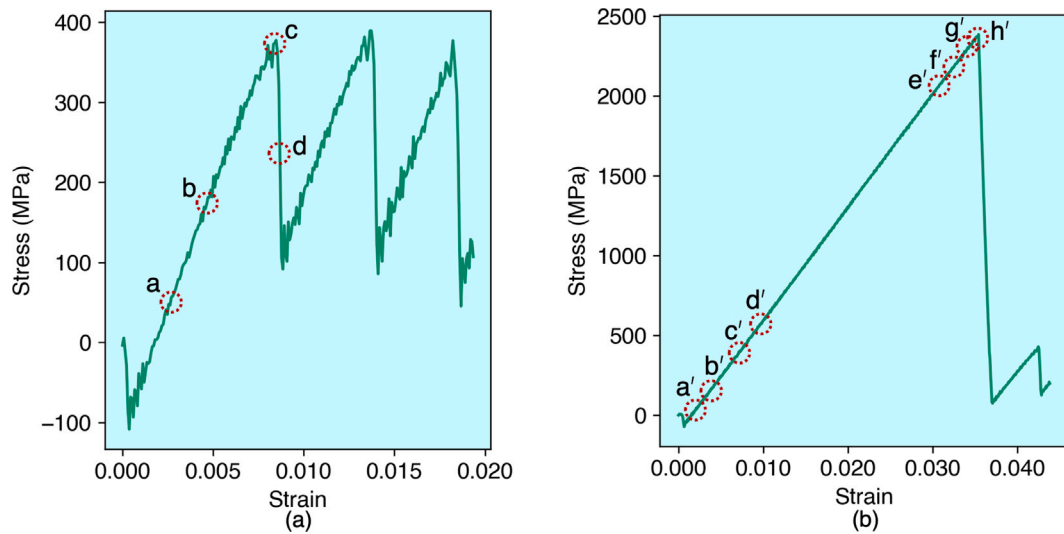
Fig. 4. Stress–strain curves for (a) an edge and (b) a screw dislocation interacting with a void with a radius of 4.8 nm in Ni.
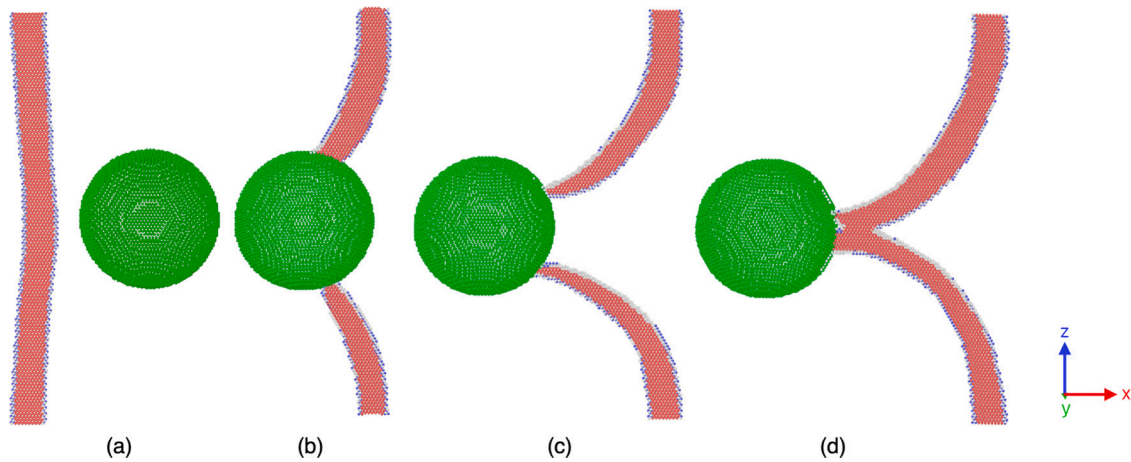

Fig. 5. A series of configurations of an edge dislocation interacting with a void with a radius of 4.8 nm in Ni, corresponding to selected points on the stress–strain curve in Fig. 4(a).
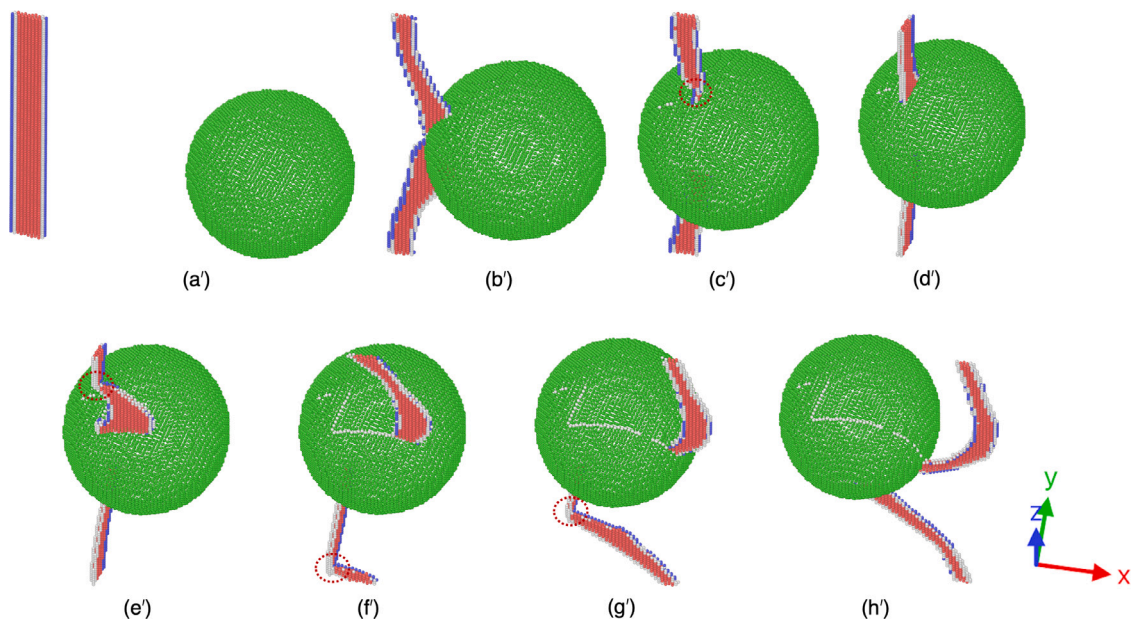

Fig. 6. A series of configurations of a screw dislocation interacting with a void with a radius of 4.8 nm in Ni, corresponding to selected points on the stress–strain curve in Fig. 4(b). The red circles in (c') and (e'–g') mark local cross-slips.
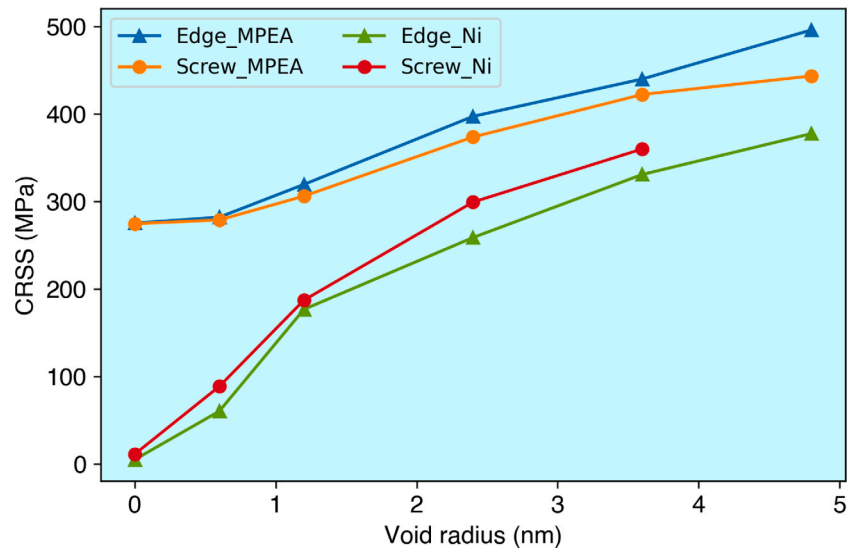
Fig. 7. CRSS values (in MPa) for Ni and the MPEA as a function of the void radius. The CRSS for the screw dislocation interacting with a 4.8 nm void in Ni is not shown because it is much higher, i.e., 2385.1 MPa.
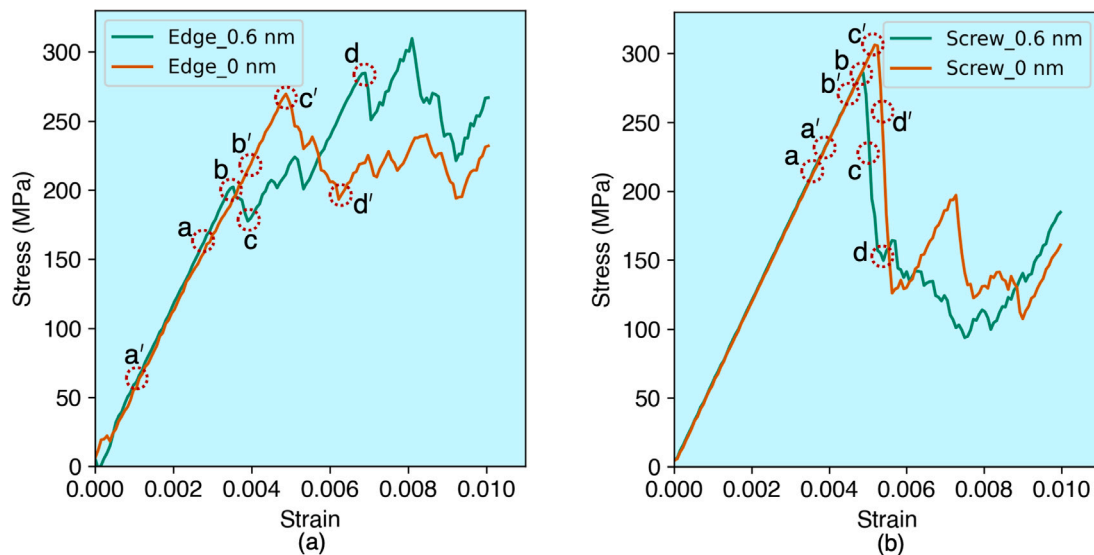

Fig. 8. Stress–strain curves for (a) an edge and (b) a screw dislocation interacting with a void with a radius of 0.6 nm in the MPEA. The curves for the void-free cases are also shown and labeled as "0 nm".

dislocation moves continuously until it makes contact with the void before bypassing it. Once the dislocation exits the void – at a peak stress – there is a pronounced drop in stress. The maximum stress reached during this interaction, which is effectively the stress required for the dislocation to exit the void, is defined as the CRSS. In terms of the bypassing mechanism, all dislocations bypass the void by shearing on the original {111} plane, except when a screw dislocation interacts with a 4.8 nm void, where a series of local cross-slip occurs near the void surface, as shown in Fig. 6. Because of the cross-slip, a very high CRSS, 2385.1 MPa, is reached, which is substantially higher than that for the edge dislocation interacting with the same void, i.e., 377.6 MPa. Our finding that smaller voids can be more easily bypassed by simple shearing of a screw dislocation without cross-slip is aligned with a previous work [49].

As the void radius increases, the CRSS increases, as summarized in Fig. 7. For the edge dislocation, the lowest CRSS (60.5 MPa) is observed for a void with a radius of 0.6 nm, while the screw dislocation exhibits the minimum CRSS of 88.8 MPa under the same condition. The void-to-lattice ratio in CRSS is 11.72 for the edge dislocation and 7.81 for

the screw dislocation, highlighting the pronounced strengthening effect of even a very small void on the dislocation glide in Ni. When the void radius increases from 0.6 nm to 3.6 nm, the CRSS increases by 5.47 times for the edge dislocation and 4.06 times for the screw dislocation. It is also evident that the screw dislocation requires a higher CRSS to overcome the void than does the edge dislocation. However, the screw-to-edge radius in CRSS is 1.09 for a 3.6 nm void and 1.47 for a 0.6 nm void, both of which are lower than that (2.2) for a dislocation glide in a void-free lattice. This trend suggests that introducing a void homogenizes the plastic deformation of different dislocation types.

3.2. MPEA

The stress–strain responses for a single dislocation interacting with a 0.6 nm void in the MPEA are shown in Fig. 8. The curves for the dislocation glide in a void-free lattice are also shown. Selected dislocation configurations are shown in Figs. 9–12. For the 4.8 nm void, the stress–strain curves are presented in Fig. 13, and the selected dislocation configurations are illustrated in Figs. 14 and 15. While
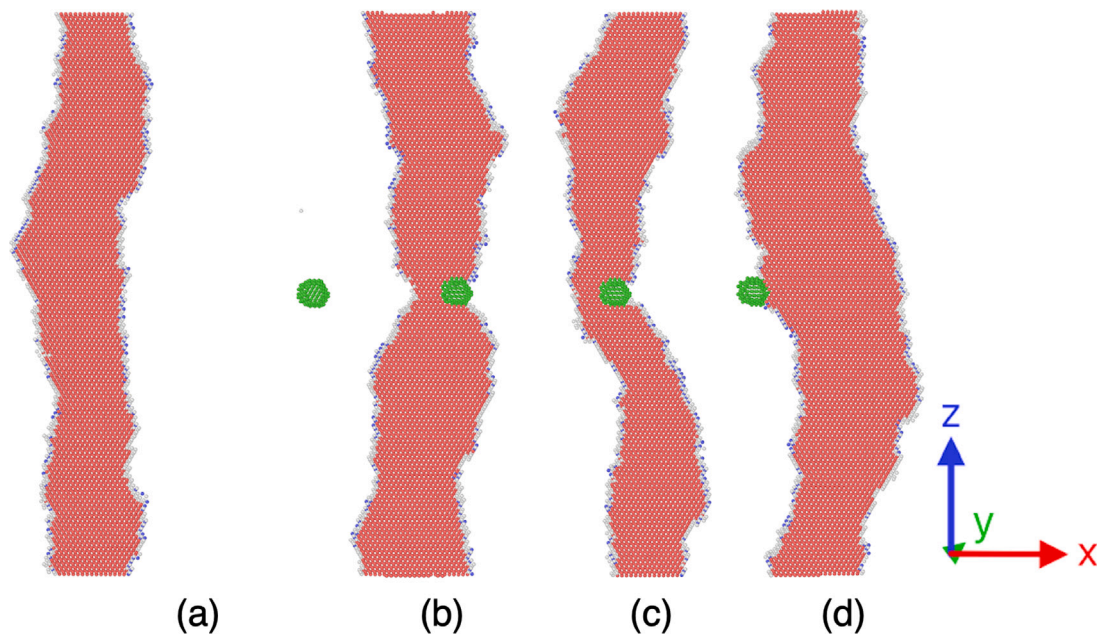
Fig. 9. A series of configurations of an edge dislocation interacting with a void with a radius of 0.6 nm in the MPEA, corresponding to selected points on the green stress–strain curve in Fig. 8(a).
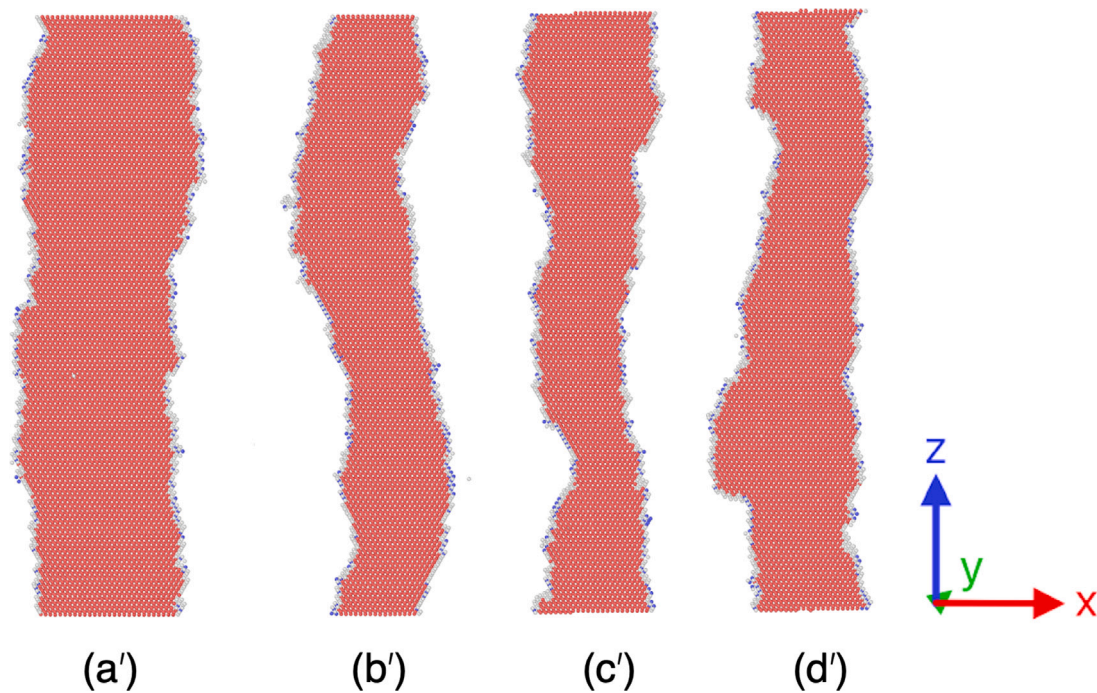

Fig. 10. A series of configurations of an edge dislocation gliding in a void-free MPEA, corresponding to selected points on the orange stress–strain curve in Fig. 8(a).

the dislocation is attracted to the void in the MPEA, this attraction is insufficient to move the dislocation in the MPEA lattice, in contrast to Ni. Thus, unlike Ni, no negative stress is present at low strains for any void size in the MPEA.

To better understand the dislocation/void interactions, we first assess the dislocation glide in a void-free lattice. In most cases, the first peak in the stress–strain curve marks the point at which the dislocation begins moving. However, the detailed dislocation behavior prior to the peak differs between edge and screw dislocations. For the edge dislocation, in most cases, as measured near the central region along the dislocation line, the stacking fault contracts and then the dislocation

starts moving, which corresponds to the first peak. In some cases, however, the stacking fault contraction corresponds to a small stress drop on the stress–strain curve. For the screw dislocation, the entire line is composed of two segments, which are on different {111} planes. As the stress increases, all segments change to the xz plane where the RSS is applied. Once that happens, the screw dislocation starts to move, and the stress drops.

Similar phenomena are observed in the dislocation/void interaction simulations. For the smallest void with a radius of 0.6 nm, the void is easily sheared by the dislocation without a substantial increase in
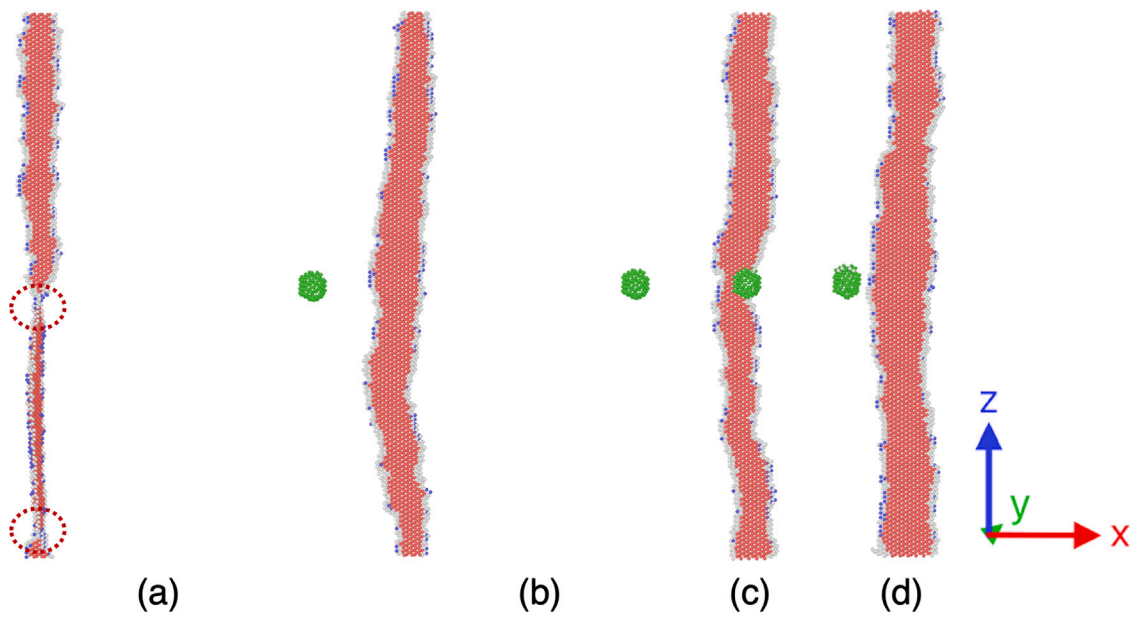
Fig. 11. A series of configurations of a screw dislocation interacting with a void with a radius of 0.6 nm in the MPEA, corresponding to selected points on the green stress–strain curve in Fig. 8(b). The red circles in (a) mark local cross-slips.
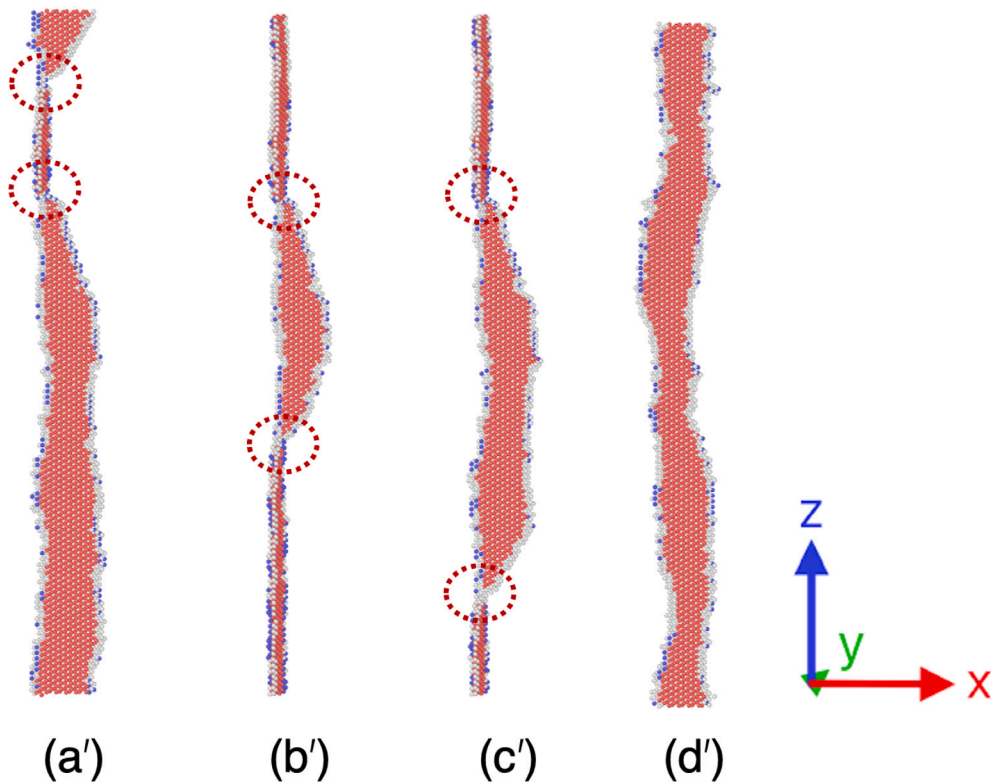

Fig. 12. A series of configurations of a screw dislocation gliding in a void-free lattice in the MPEA, corresponding to selected points on the orange stress–strain curve in Fig. 8(b). The red circles in (a'–c') mark local cross-slips.

the stress once the dislocation starts moving. As a result, the void-to-lattice ratios in the CRSS – 1.025 for the edge and 1.02 for the screw – are much lower than those in Ni. The diminished void-induced strengthening in the MPEA agrees with a previous finding that the irradiation hardening is lower in MPEAs than in pure metals [50]. For larger voids, a stress increase is observed when the dislocation becomes in contact with the void, as shown in Fig. 13. It follows that the dislocation shears the void and exits it, at which point a large

stress drop is incurred. For the screw dislocation, cross-slip occurs in the largest void which has a radius of 4.8 nm. Unlike in Ni, it only happens very locally near the void surface, as shown in Fig. 15(b'), as a result of the MPEA's lower ISFE.

As shown in Fig. 7, (i) introducing a void consistently increases the CRSS in the MPEA, and (ii) an increase in the void radius increases the CRSS, as in Ni. However, the amount of increase is substantially smaller compared with Ni. For example, as the void radius increases
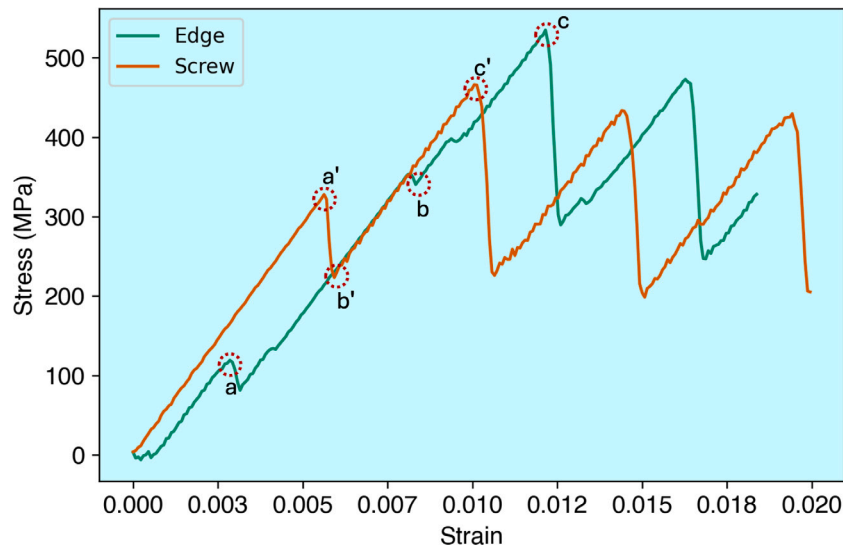
Fig. 13. Stress–strain curves for an edge and a screw dislocation interacting with a void with a radius of 4.8 nm in the MPEA.
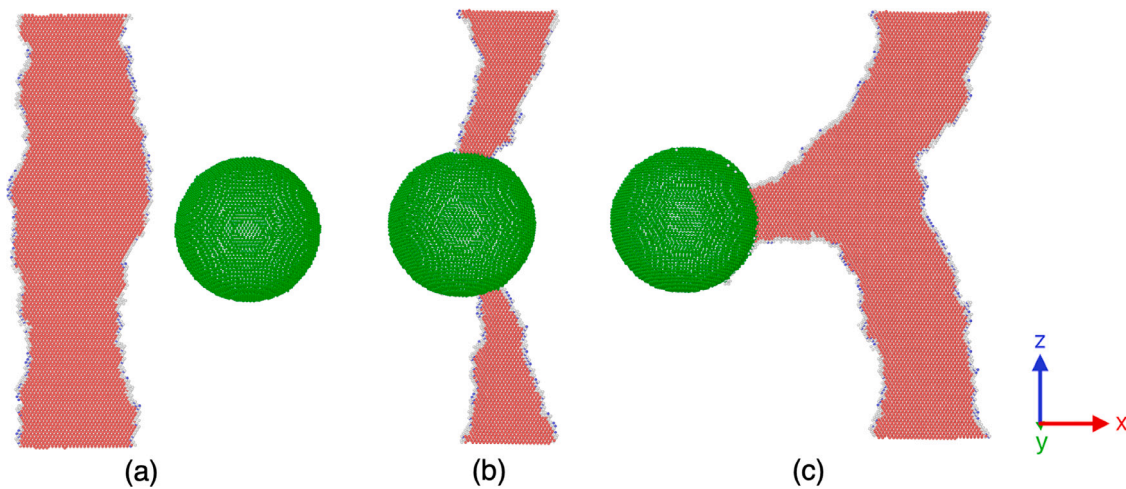

Fig. 14. A series of configurations of an edge dislocation interacting with a void with a radius of 4.8 nm in the MPEA, corresponding to selected points on the green stress–strain curve in Fig. 13.

from 0.6 nm to 3.6 nm, the CRSS increases by 1.56 times for the edge dislocation and 1.51 times for the screw dislocation, which are much smaller than 5.47 and 4.06 in Ni. Concurrently, the MPEA-to-Ni ratios in CRSS significantly drop as the void size increases. For the 0.6 nm void, the ratios are 4.66 for the edge dislocation and 3.14 for the screw dislocation; for the 3.6 nm void, the ratios are 1.33 and 1.17, respectively. These ratios are substantially lower than those for a void-free lattice: 53.37 and 24.16. These observations suggest that while the void makes dislocation dynamics more difficult in both Ni and MPEA, the interactions are much less sensitive to the void size in MPEA than in Ni. Effectively, the presence of a void reduces the disparities in dislocation dynamics between the two materials. Finally, the screw-to-edge ratios in CRSS are below unity, specifically 0.96 and 0.99 for the 3.6 nm and 0.6 nm voids, respectively. These results match the same ratio for the void-free lattice glide in the MPEA (0.997).

4. Conclusions

In the present work, we use atomistic simulations to explore how a dislocation interacts with a void, and to shed light on the contrasting behaviors observed in Ni versus the MPEA. In pure Ni, even a relatively small void can cause a marked increase in the CRSS, and the largest

void (with a 4.8 nm radius) is found to induce cross-slip in the screw dislocation. Conversely, the MPEA exhibits only a slight increase in CRSS for a small void, a moderate CRSS increase for a larger void, with the largest void prompting merely localized cross-slip near its surfaces. As a result, a void plays a much smaller role in affecting dislocation dynamics in the MPEA than in Ni. We also find that the screw-to-edge ratio in CRSS, regardless of whether the void is present or not, is less than unity in the MPEA, in contrast to Ni.

Overall, our findings emphasize the crucial role that local chemical environments and atomic-scale defect interactions play in defining the mechanical properties of both pure metals and complex alloys. In the MPEA, the energy landscape experienced by moving dislocations is considerably more varied than in Ni, leading to distinct slip behaviors. By analyzing dislocation behavior using atomistic simulations, this work provides valuable guidance for designing next-generation alloys that effectively combine compositional complexity with tailored nanostructural features to enhance strength, ductility, and overall performance.

Previous experiments have compared mechanical properties and deformation mechanisms in MPEAs and pure metals that contain voids. For instance, Gao et al. [51] demonstrated via in situ transmission electron microscopy that void coalescence in both MPEAs and pure metals
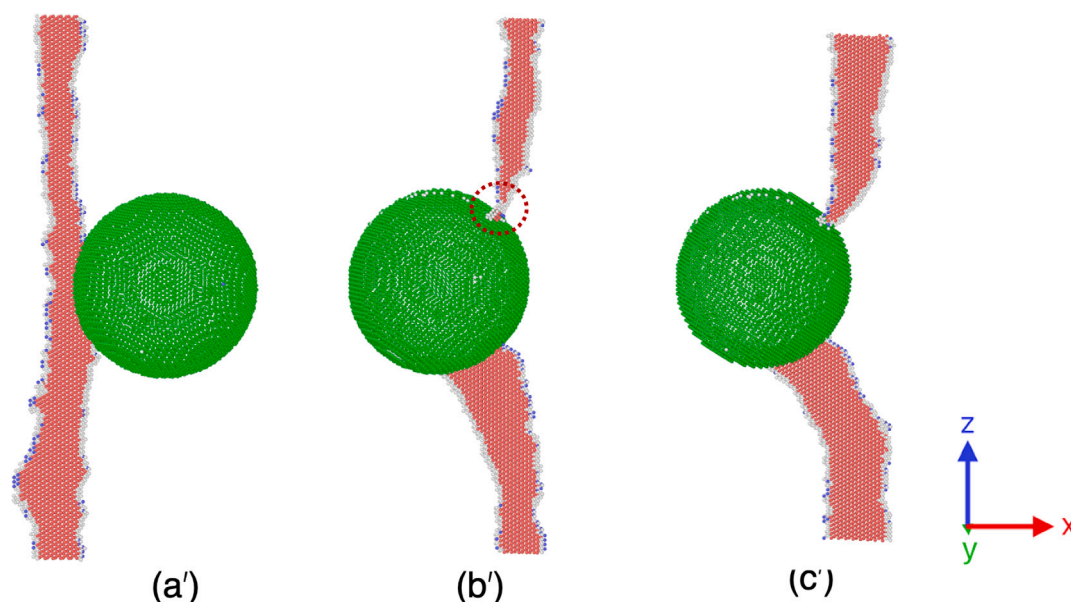
Fig. 15. A series of configurations of a screw dislocation interacting with a void with a radius of 4.8 nm in the MPEA, corresponding to selected points on the orange stress–strain curve in Fig. 13. The red circle in (b') marks a local cross-slip.

can propagate by relative shearing along the boundary of nanotwins in the ligament between voids. Lu et al. [52] further showed that pre-existing dislocations and local lattice distortions in MPEAs significantly affect void swelling and defect evolution under irradiation, highlighting the unique defect interactions in MPEAs compared to pure metals. These studies emphasize the importance of defect/void interactions across scales and motivate future multiscale computational work.

CRediT authorship contribution statement

Anshu Raj: Writing – original draft, Visualization, Software, Methodology, Investigation, Formal analysis, Data curation. **Weisen Ji:** Visualization. **Shuozhi Xu:** Writing – review & editing, Validation, Supervision, Project administration, Methodology, Funding acquisition, Conceptualization.

Declaration of competing interest

The authors declare that they have no known competing financial interests or personal relationships that could have appeared to influence the work reported in this paper.

Acknowledgments

Data availability

The datasets generated and/or analyzed during the current study are available in this GitHub repository: https://github.com/shuozhixu/JAC_2025.

References

[1] I.J. Beyerlein, S. Xu, J. Llorca, J.A. El-Awady, J.R. Mianroodi, B. Svendsen, Alloy design for mechanical properties: Conquering the length scales, MRS Bull. 44 (2019) 257–265.

[2] H.Y. Diao, R. Feng, K.A. Dahmen, P.K. Liaw, Fundamental deformation behavior in high-entropy alloys: An overview, Curr. Opin. Solid State Mater. Sci. 21 (2017) 252–266.

[3] X. Li, K. Lu, Playing with defects in metals, Nat. Mater. 16 (2017) 700–701.

[4] Y. Ye, Q. Wang, J. Lu, C. Liu, Y. Yang, High-entropy alloy: challenges and prospects, Mater. Today 19 (2016) 349–362.

[5] J.W. Yeh, S.K. Chen, S.J. Lin, J.Y. Gan, T.S. Chin, T.T. Shun, C.H. Tsau, S.Y. Chang, Nanostructured high-entropy alloys with multiple principal elements: novel alloy design concepts and outcomes, Adv. Eng. Mater. 6 (2004) 299–303.

[6] B. Cantor, I.T.H. Chang, P. Knight, A.J.B. Vincent, Microstructural development in equiatomic multicomponent alloys, Mater. Sci. Eng. A 375–377 (2004) 213–218.

[7] E.J. Pickering, N.G. Jones, High-entropy alloys: a critical assessment of their founding principles and future prospects, Int. Mater. Rev. 61 (2016) 183–202.

[8] A. Takeuchi, K. Amiya, T. Wada, K. Yubuta, W. Zhang, High-entropy alloys with a hexagonal close-packed structure designed by equi-atomic alloy strategy and binary phase diagrams, JOM 66 (2014) 1984–1992.

[9] E.P. George, D. Raabe, R.O. Ritchie, High-entropy alloys, Nat. Rev. Mater. 4 (2019) 515–534.

[10] O.N. Senkov, D.B. Miracle, K.J. Chaput, J.-P. Couzinie, Development and exploration of refractory high entropy alloys—a review, J. Mater. Res. 33 (2018) 3092–3128.

[11] S. Mubassira, M. Fani, A. Raj, C. Hirt, R.S. Brinlee, A. Poozesh, W.-R. Jian, S.Z. Chavoshi, C. Lee, S. Xu, Chemical short-range order and its influence on selected properties of non-dilute random alloys, Comput. Mater. Sci. 248 (2025) 113587.

[12] Z. Li, K.G. Pradeep, Y. Deng, D. Raabe, C.C. Tasan, Metastable high-entropy dual-phase alloys overcome the strength–ductility trade-off, Nature 534 (2016) 227–230.

[13] E. Ma, Unusual dislocation behavior in high-entropy alloys, Scr. Mater. 181 (2020) 127–133.

[14] Y. Zhang, T.T. Zuo, Z. Tang, M.C. Gao, K.A. Dahmen, P.K. Liaw, Z.P. Lu, Microstructures and properties of high-entropy alloys, Prog. Mater. Sci. 61 (2014) 1–93.

[15] M. Li, J. Gazquez, A. Borisevich, R. Mishra, K.M. Flores, Evaluation of microstructure and mechanical property variations in Al_xCoCrFeNi high entropy alloys produced by a high-throughput laser deposition method, Intermetallics 95 (2018) 110–118.

[16] A. Sharma, G. Balasubramanian, Dislocation dynamics in $Al_{0.1}$CoCrFeNi high-entropy alloy under tensile loading, Intermetallics 91 (2017) 31–34.

[17] M.A.A. Hasan, S. Shin, P.K. Liaw, Short-range order effects on the thermodynamic behavior of Al_xCoCrFeNi high-entropy alloys, Comput. Mater. Sci. 239 (2024) 112980.

[18] Y.-C. Yang, C. Liu, C.-Y. Lin, Z. Xia, The effect of local atomic configuration in high-entropy alloys on the dislocation behaviors and mechanical properties, Mater. Sci. Eng. A 815 (2021) 141253.

[19] D. Li, Y. Zhang, The ultrahigh charpy impact toughness of forged Al$_x$CoCrFeNi high entropy alloys at room and cryogenic temperatures, Intermetallics 70 (2016) 24–28.

[20] Y. Wu, Y. Yue, X. Yan, C. Zhang, J. Huang, P.K. Liaw, Y. Zhang, Mechanical and corrosion behavior of CoCrFeNiAl$_{0.3}$ high entropy alloy seamless tubes, J. Alloys Compd. 1010 (2025) 177143.

[21] X. Ma, W. Zhang, F. Zhu, L. Song, Q. Zhang, The effect of Al in Al$_{0.3}$CoCrFeNi alloy on the damage accumulation at different temperatures, J. Nucl. Mater. 600 (2024) 155283.

[22] Z. Sun, C. Shi, C. Liu, H. Shi, J. Zhou, The effect of short-range order on mechanical properties of high entropy alloy Al$_{0.3}$CoCrFeNi, Mater. Des. 223 (2022) 111214.

[23] A. Raj, S. Mubassira, S. Xu, Generalized stacking fault energies and local slip resistances in Al$_{0.3}$CoCrFeNi: An atomistic study, High Entropy Alloy. Mater. 3 (2025) 203–214.

[24] A. Raj, J. Brechtl, S. Mubassira, P.K. Liaw, S. Xu, Dislocation glide in Al$_{0.3}$CoCrFeNi: Insights from molecular dynamics and statistical analysis, Mater. Lett. 400 (2025) 139038.

[25] Y. Osetsky, D. Bacon, Void and precipitate strengthening in α-iron: what can we learn from atomic-level modelling? J. Nucl. Mater. 323 (2003) 268–280.

[26] D. Bacon, Y. Osetsky, Modelling dislocation–obstacle interactions in metals exposed to an irradiation environment, Mater. Sci. Eng.: A 400–401 (2005) 353–361.

[27] X. Ma, H. Zhai, L. Song, W. Zhang, Y. Hu, Q. Zhang, In situ study on plastic deformation mechanism of Al$_{0.3}$CoCrFeNi high-entropy alloys with different microstructures, Mater. Sci. Eng.: A 857 (2022) 144134.

[28] R. Scattergood, D. Bacon, The strengthening effect of voids, Acta Metall. 30 (1982) 1665–1677.

[29] D. Terentyev, D.J. Bacon, Y.N. Osetsky, Interaction of an edge dislocation with voids in α-iron modelled with different interatomic potentials, J. Phys.: Condens. Matter. 20 (2008) 445007.

[30] M. Fani, L. Cervantes, A. Raj, S. Xu, Effects of irradiation-induced voids on confined layer slips in metallic nanolaminates, J. Chem. Phys. 161 (2024) 214702.

[31] Y.N. Osetsky, D.J. Bacon, Atomic-scale mechanisms of void hardening in bcc and fcc metals, Phil. Mag. 90 (2010) 945–961.

[32] A. Simar, H.-J.L. Voigt, B.D. Wirth, Molecular dynamics simulations of dislocation interaction with voids in nickel, Comput. Mater. Sci. 50 (2011) 1811–1817.

[33] Y. Cheng, E. Bitzek, D. Weygand, P. Gumbsch, Atomistic simulation of dislocation–void interactions under cyclic loading, Modelling Simul. Mater. Sci. Eng. 18 (2010) 025006.

[34] T. Okita, K. Asari, S. Fujita, M.I. and, Effect of the stacking fault energy on interactions between an edge dislocation and a spherical void in fcc metals at various spatial geometries, Fusion Sci. Technol. 66 (2014) 289–294.

[35] S. Hayakawa, K. Doihara, T. Okita, M. Itakura, M. Aichi, K. Suzuki, Screw dislocation–spherical void interactions in fcc metals and their dependence on stacking fault energy, J. Mater. Sci. 54 (2019) 11509–11525.

[36] K. Asari, O. Hetland, S. Fujita, M. Itakura, T. Okita, The effect of stacking fault energy on interactions between an edge dislocation and a spherical void by molecular dynamics simulations, J. Nucl. Mater. 442 (2013) 360–364.

[37] K. Doihara, T. Okita, M. Itakura, M. Aichi, K.S. and, Atomic simulations to evaluate effects of stacking fault energy on interactions between edge dislocation and spherical void in face-centred cubic metals, Phil. Mag. 98 (2018) 2061–2076.

[38] W.-R. Jian, M. Zhang, S. Xu, I.J. Beyerlein, Atomistic simulations of dynamics of an edge dislocation and its interaction with a void in copper: a comparative study, Modelling Simul. Mater. Sci. Eng. 28 (2020) 045004.

[39] P. Jing, T. Khraishi, J.A. Young, B.D.W. and, Multi-scale simulations of the effects of irradiation-induced voids and helium bubbles on the mechanical properties of aluminium, Phil. Mag. 85 (2005) 757–767.

[40] T. Hatano, T. Kaneko, Y. Abe, H. Matsui, Void-induced cross slip of screw dislocations in fcc copper, Phys. Rev. B 77 (2008) 064108.

[41] M. Bahramyan, R.T. Mousavian, D. Brabazon, Molecular dynamic simulation of edge dislocation-void interaction in pure Al and Al-Mg alloy, Mater. Sci. Eng.: A 674 (2016) 82–90.

[42] Y.-K. Dou, H. Cao, X.-F. He, J. Gao, J. li Cao, W. Yang, Interaction mechanism of an edge dislocation with a void in Fe-Ni-Cr concentrated solid-solution alloy, J. Alloys Compd. 857 (2021) 157556.

[43] X. Mei, Y. Xu, Y. Zhu, L. Zhao, Z. Li, M. Huang, The statistic and fluctuant phenomena of interaction between edge extended dislocation and microvoid in FCC CoCrFeCuNi high entropy alloy, J. Nucl. Mater. 568 (2022) 153884.

[44] A. Vaid, M. Zaiser, E. Bitzek, Atomistic simulations of dislocation-void interactions in concentrated solid solution alloys, Metals 13 (2023) 1655.

[45] D. Farkas, A. Caro, Model interatomic potentials for Fe-Ni-Cr-Co-Al high-entropy alloys, J. Mater. Res. 35 (2020) 3031–3040.

[46] A.P. Thompson, H.M. Aktulga, R. Berger, D.S. Bolintineanu, W.M. Brown, P.S. Crozier, P.J. in 't Veld, A. Kohlmeyer, S.G. Moore, T.D. Nguyen, R. Shan, M.J. Stevens, J. Tranchida, C. Trott, S.J. Plimpton, Lammps - a flexible simulation tool for particle-based materials modeling at the atomic, meso, and continuum scales, Comput. Phys. Comm. 271 (2022) 108171.

[47] P. Hirel, Atomsk: A tool for manipulating and converting atomic data files, Comput. Phys. Comm. 197 (2015) 212–219.

[48] A. Stukowski, Visualization and analysis of atomistic simulation data with OVITO — the open visualization tool, Modelling Simul. Mater. Sci. Eng. 18 (2009) 015012.

[49] T. Hatano, T. Kaneko, Y. Abe, H. Matsui, Void-induced cross slip of screw dislocations in FCC copper, Phys. Rev. B 77 (2008) 064108.

[50] Y. Chen, S. Wang, H. Feng, W. Li, B. Liu, J. Li, Y. Liu, P.K. Liaw, Q. Fang, Irradiation hardening behavior of high entropy alloys using random field theory informed discrete dislocation dynamics simulation, Int. J. Plast. 162 (2023) 103497.

[51] B. Gao, Q. Xiang, T. Guo, X. Guo, S. Tang, X.X. Huang, In situ TEM investigation on void coalescence in metallic materials, Mater. Sci. Eng. A 734 (2018) 260–268.

[52] C. Lu, T. Yang, K. Jin, G. Velisa, P. Xiu, M. Song, Q. Peng, F. Gao, Y. Zhang, H. Bei, W.J. Weber, L. Wang, Enhanced void swelling in NiCoFeCrPd high-entropy alloy by indentation-induced dislocations, Mater. Res. Lett. 6 (2018) 584–591.